

Monoesterase Activity of a Purple Acid Phosphatase Mimic with a Cyclam Platform

Peter Comba,^{*,[a]} Lawrence R. Gahan,^[b] Graeme R. Hanson,^[c] Valeriu Mereacre,^[d] Christopher J. Noble,^[c] Annie K. Powell,^[d] Ion Prisecaru,^[e] Gerhard Schenk,^[b, f] and Marta Zajaczkowski-Fischer^[a]

Abstract: The synthesis and characterization of a novel dinucleating ligand L (L = 4,11-dimethyl-1,8-bis[2-[N-(di-2-pyridylmethyl)amino]ethyl]cyclam) and its μ -oxo-bridged diferric complex $[(H_2L)\{Fe^{III}_2(O)\}(Cl)_4]^{2+}$ are reported. This diiron(III) complex is the first example of a truly functional purple acid phosphatase (PAP) mimic as it accelerates the hydrolysis of the activated phosphomonoester 2,4-dinitrophenyl

phosphate (DNPP). The spectroscopic and kinetic data indicate that only substrates that are monodentately bound to one of the two ferric ions can be attacked by a suitable nucleophile. This is, most probably, a terminal iron(III)-

bound hydroxide. DFT calculations support this assumption and also highlight the importance of secondary interactions, exerted by the protonated cyclam platform, for the positioning and activation of the iron(III)-bound substrate. Similar effects are postulated in the native enzyme but addressed in PAP mimics for the first time.

Keywords: bioinorganic chemistry • enzymes • hydrogen bonds • hydrolysis • iron

Introduction

The hydrolysis of carboxylic esters, amides, and mono-, di-, and triesters of phosphates in biological systems is generally catalyzed by metallohydrolases with dinuclear metal sites. The wide variety of enzymes, the extensive model chemistry, and possible applications of the metalloproteins and func-

tional models in medicinal and environmental chemistry have been reviewed.^[1,2] Computational^[3-6] and low-molecular-weight experimental models^[2,7,8] together with an impressive amount of structural,^[9] spectroscopic,^[10,11] and kinetic data^[2,12] on enzymes, mutants, and models have helped to develop a detailed understanding of the reaction mechanisms of hydrolases in general and, in particular, of the purple acid phosphatases (PAPs), the class of enzymes addressed here on the basis of a novel low-molecular-weight model system. PAPs with molecular weights of between 30 and 90 kDa have been isolated from mammals, plants, and microorganisms. They catalyze the hydrolysis of a range of phosphorylated substrates in the pH range of 3.0 to 8.0, have a heterovalent $Fe^{III}-M^{II}$ ($M = Fe, Zn, \text{ or } Mn$) active site (the characteristic purple color, $\lambda_{max} = 510-560 \text{ nm}$, $\epsilon = 3000-4000 \text{ M}^{-1} \text{ cm}^{-1}$, arises from a tyrosine-to- Fe^{III} charge-transfer (CT) transition), and the biological role may also include iron transport and the generation of reactive oxygen species in the case of mammalian PAPs.^[1,2,8,9] Important structural features of the PAP active site (Scheme 1), derived from crystallographic and spectroscopic data as well as from mechanistic studies, include 1) a bridging hydroxide (or oxo anion) and 2) noncoordinated histidine groups, which may help to position the substrate.^[15] These structural features have not yet been addressed in model chemistry.^[16] Moreover, the important physiological role of PAPs in hydrolyzing phosphomonoesters has not been achieved by any current model complex. We hypothesized that secondary interactions may be required to position the monoester substrate such that a bridging coordination mode in which the substrate is not accessible to nucleophilic attack by a terminal hydroxide (see below)^[14,17] is prevented. The design of our

[a] Prof. Dr. P. Comba, Dr. M. Zajaczkowski-Fischer
Anorganisch-Chemisches Institut, Universität Heidelberg
INF 270, 69120 Heidelberg (Germany)
Fax: (+49)6221-546617
E-mail: peter.comba@aci.uni-heidelberg.de

[b] Prof. Dr. L. R. Gahan, Prof. Dr. G. Schenk
School of Chemistry and Molecular Biosciences
The University of Queensland
Brisbane, Queensland 4072 (Australia)

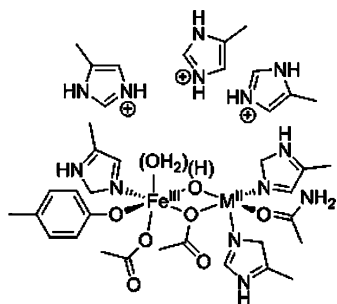
[c] Prof. Dr. G. R. Hanson, Dr. C. J. Noble
Centre for Advanced Imaging
The University of Queensland
Brisbane, Queensland 4072 (Australia)

[d] Dr. V. Mereacre, Prof. Dr. A. K. Powell
Institut für Anorganische Chemie
Karlsruher Institut für Technologie
Engesserstrasse 15, 76131 Karlsruhe (Germany)

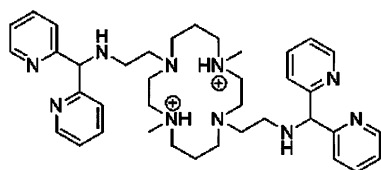
[e] I. Prisecaru
National Institute for Materials Physics, Magnetism Laboratory
Bucharest (Romania)

[f] Prof. Dr. G. Schenk
Department of Chemistry
National University of Ireland – Maynooth
Maynooth, Co. Kildare (Ireland)

Supporting information for this article is available on the WWW under <http://dx.doi.org/10.1002/chem.201100229>.



Scheme 1. Schematic representation of the active site of PAPs at physiological pH ($M^{\text{II}} = \text{Fe}^{\text{II}}, \text{Zn}^{\text{II}}, \text{Mn}^{\text{II}}$; His, Tyr, and Glu amino acid side-chains are abbreviated as imidazole, phenolate, and carboxylate, respectively).^[13,14]



Scheme 2. Structure of the ligand H_2L^{2+} .

dinucleating ligand H_2L^{2+} (Scheme 2) is therefore based on a cyclam platform with two appended tridentate coordination sites, with the protonated amines of the macrocycle expected to help stabilize a monodentate phosphoester (see below for the DFT-based ligand design).^[18] Herein, we report the DFT-based ligand design, the syntheses of the ligand H_2L^{2+} and its diferric complex, an extensive characterization of the corresponding solution chemistry based on various spectroscopic methods (solution structural characterization of the various species in equilibrium), and the kinetic analysis of phosphate ester hydrolysis.

Results and Discussion

Ligand design: Preliminary DFT calculations confirmed H_2L^{2+} as a suitable ligand for the formation of dinuclear Fe^{III} complexes as a functional PAP model system. Relaxed potential energy surface (PES) scans were performed for the reac-

tion of the oxo-bridged diferric complex of H_2L^{2+} with one monodentately coordinated DNPP substrate molecule, $[(\text{H}_x\text{L})\{\text{Fe}^{\text{III}}_2(\text{O})\}(\text{OH})_2(\text{OH}_2)(\text{DNPP})] (x=2, 0; \text{DNPP} = 2,4\text{-dinitrophenyl phosphate})$, which leads, on one hand, to bridging coordination of the substrate (that is, reversible inactivation of the monoester substrate; see Figure 1, left-hand side) and, on the other, to the hydrolysis product (bridging coordination of phosphate; see Figure 1, right-hand side). PES scans for both reactions were performed with the fully deprotonated ligand and with the doubly protonated cyclam platform to model the influence of the assumed hydrogen-bonding interactions. For both models, the approximate activation barrier for the bridging mode (inhibition) is considerably larger (39.1 and 50.2 kJ mol^{-1} with and without hydrogen bonding, respectively) than for the hydrolysis reaction (3.1 and 20.6 kJ mol^{-1}). With hydrogen bonding between DNPP and cyclam included (black curves in Figure 1), a nearly barrierless hydrolysis emerges. These preliminary calculations indicate that 1) an oxo-bridged diferric complex of H_2L^{2+} is able to form hydrogen bonds to phosphoesters, 2) there are steric interactions that lead to a preference for monodentate substrate binding, and 3) the hydrogen bonds help to facilitate the hydrolysis reaction.

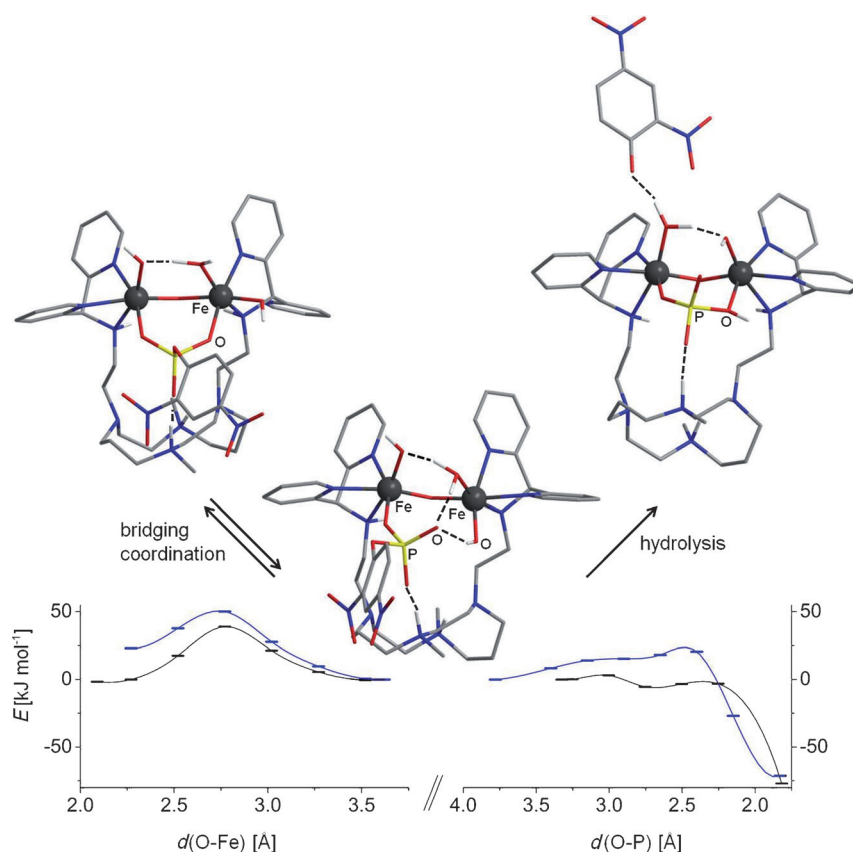
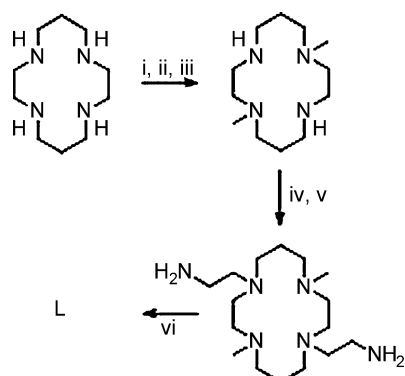


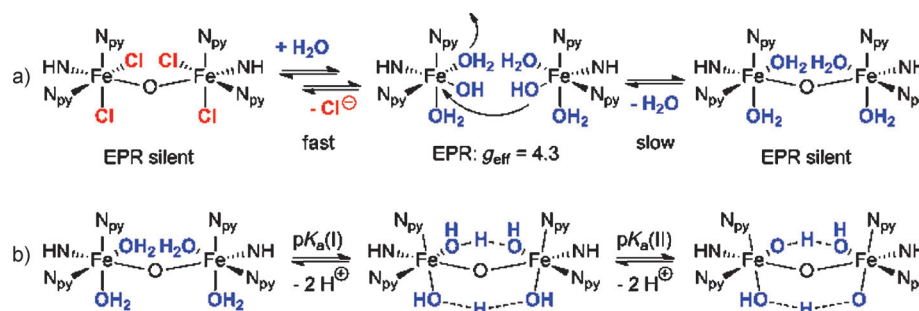
Figure 1. Calculated structures and energy profiles (relaxed PES scans) for bridging coordination (left side) and hydrolysis of DNPP (right side) with $[(\text{H}_x\text{L})\{\text{Fe}^{\text{III}}_2(\text{O})\}(\text{OH})_2(\text{OH}_2)]^{x+}$ ($x=2$ (hydrogen bonding, black curves) and $x=0$ (hypothetical, no hydrogen bonding, blue curves); calculations performed at the B3LYP/LanL2dz level of theory).

Ligand synthesis and coordination chemistry: The dinucleating cyclam derivative L was prepared by standard procedures in a six-step synthesis starting from cyclam in an overall yield of 14% (see Scheme 3). Reaction of the ligand with



Scheme 3. Synthesis of ligand L. Reagents: i) CH_2O , H_2O ; ii) MeI, MeCN; iii) NaOH, CHCl_3 ; iv) *N*-tosylaziridine, MeCN; v) conc. H_2SO_4 , Et_2O , NaOH, CHCl_3 ; vi) di-2-pyridylmethyl chloride, K_2CO_3 , MeCN.

$(\text{NEt}_4)[\text{FeCl}_4]^{[19]}$ in acetonitrile under an ambient atmosphere yielded a symmetrical oxo-bridged diiron(III) complex with two terminal chlorides at each Fe^{III} center. ESI-MS (see Figure 2) and titrations monitored by electronic and NMR spectroscopy (see the Supporting Information) indicated that $[(\text{H}_2\text{L})\{\text{Fe}^{\text{III}}_2(\text{O})\}(\text{Cl})_4]^{2+}$ is the only species formed in solution.



Scheme 4. a) Proposed reactions after the addition of buffer to a solution of $[(\text{H}_2\text{L})\{\text{Fe}^{\text{III}}_2(\text{O})\}(\text{Cl})_4]^{2+}$ in MeCN. b) Proposed protonation equilibria of $[(\text{H}_2\text{L})\{\text{Fe}^{\text{III}}_2(\text{O})\}(\text{OH}_2)_4]^{6+}$. All iron centers are high-spin Fe^{III} .

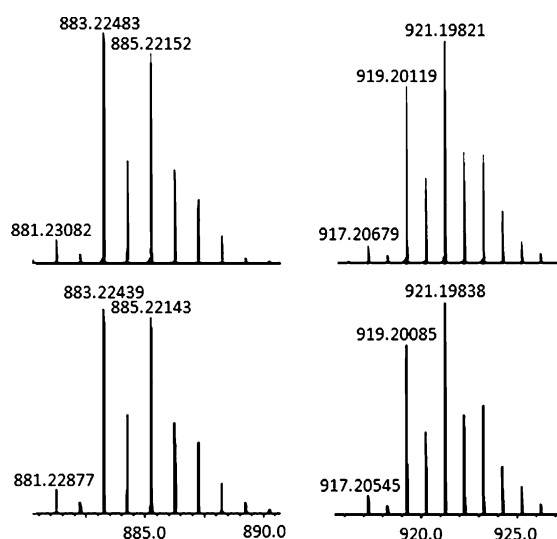


Figure 2. Isotope patterns of the experimental (top: MeCN, 1% H_2O) and calculated mass spectra (bottom) of $[\text{LFe}^{\text{III}}_2\text{Cl}_3\text{O}]^+$ (left: m/z : 883.22483) and $[\text{HLFe}^{\text{III}}_2\text{Cl}_4\text{O}]^+$ (right: m/z : 921.19821).

The NMR titrations revealed that, as expected, the two Fe^{III} ions are coordinated by the pyridine and secondary amine donors and not by the cyclam ring. The electronic absorption spectra revealed oxo-to- Fe^{III} charge-transfer transitions in a $\text{Fe}^{\text{III}}-\mu\text{-O}-\text{Fe}^{\text{III}}$ moiety, which, as expected from a strongly exchange-coupled species, is EPR silent. In 1:1 MeCN/aqueous buffer solutions time-resolved UV/Vis (see the Supporting Information) and EPR spectroscopy suggested that $[(\text{H}_2\text{L})\{\text{Fe}^{\text{III}}_2(\text{O})\}(\text{Cl})_4]^{2+}$ was hydrolyzed with protonation and cleavage of the oxo bridge to produce mononuclear high-spin Fe^{III} centers, which over time is re-established to yield an oxo-bridged EPR-silent species with aqua/hydroxo co-ligands (Scheme 4). The addition of phosphate or (hydrolytically stable) phosphomono- and -diesters to these solutions led to significant spectroscopic changes and, depending on the pH and the nature of the substrate, one or two substrate molecules could be coordinated to the dinuclear Fe^{III} complex in a monodentate or bridging mode. This was evaluated by ESI-MS (see Table 1 and the Supporting Information) and EPR spectroscopy in combination with DFT calculations (geometry optimization and broken-symmetry cal-

Table 1. Species observed in the ESI-HRMS of $[(\text{H}_2\text{L})\{\text{Fe}^{\text{III}}_2(\text{O})\}(\text{Cl})_4]^{2+}$ with phosphate or pNPP in MeCN/buffer (pH 5).^[a]

Species	Calcd m/z	Exptl m/z	Peak height [%]
$[\text{HL}^1\text{Fe}^{\text{III}}_2(\text{HPO}_4)_2(\text{OH})]^{2+}$	486.12812	486.12784	100
$[\text{H}_2\text{L}^1\text{Fe}^{\text{III}}_2(\text{HPO}_4)_2(\text{OH})(\text{ClO}_4)]^{2+}$	536.10629	536.10619	5
$[\text{HL}^1\text{Fe}^{\text{III}}_2(\text{HPO}_4)_2(\text{OH})\text{Cl}]^+$	1007.22508	1007.22480	11
$[\text{HL}^1\text{Fe}^{\text{III}}_2(\text{HPO}_4)_2(\text{OH})(\text{ClO}_4)]^+$	1071.20474	1071.20482	15
$[\text{HL}^1\text{Fe}^{\text{III}}_2(\text{pNPP})_2(\text{OH})]^{2+}$	607.14450	607.14412	100
$[\text{LiL}^1\text{Fe}^{\text{III}}_2(\text{pNPP})_2(\text{OH})]^{2+}$	610.14859	610.14830	47
$[\text{L}^1\text{Fe}^{\text{III}}_2(\text{pNPP})_2(\text{OH})]^+$	1213.28166	1213.28025	31
$[\text{HL}^1\text{Fe}^{\text{III}}_2(\text{pNPP})_2(\text{OH})\text{Cl}]^+$	1249.25784	1249.25757	45

[a] See the Supporting Information for the original data.

culations of the coupling constants J ; see Figure 3 and Table 2), Mössbauer spectroscopy (see Figures 4 and 5 and Table 3), ^{31}P NMR titrations, and UV/Vis spectroscopy (see the Supporting Information^[20]).

The variable-temperature (1.6–16.0 K) EPR spectra of $[(\text{H}_2\text{L})\{\text{Fe}^{\text{III}}_2(\text{O})\}(\text{Cl})_4]^{2+}$ with an excess of pNPP or phos-

phate at pH 5 reveal complex spectra spanning 6000 G with a dominant set of resonances centered around $g_{\text{eff}}=2$ (Figure 3). They show that the intensity of the resonances

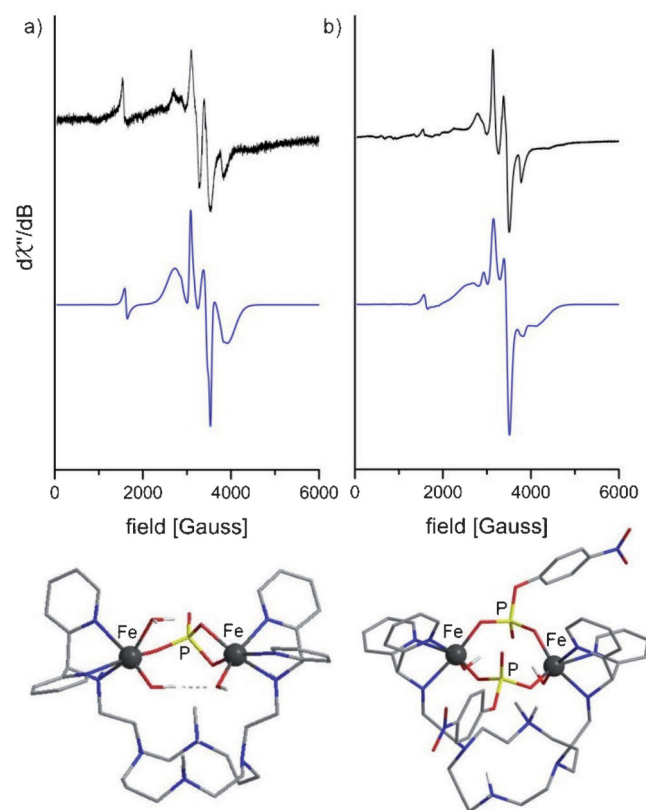


Figure 3. Experimental (black) and simulated (blue) X-band EPR spectra and calculated structures of a) $[(\text{H}_2\text{L})\{\text{Fe}^{\text{III}}_2(\text{O})\}(\text{Cl}_4)]^{2+}$ (0.5 mM) and phosphate (10 mM) in MeCN/aq. buffer (pH 5, 1.7 K, 9.37824 GHz) and b) $[(\text{H}_2\text{L})\{\text{Fe}^{\text{III}}_2(\text{O})\}(\text{Cl}_4)]^{2+}$ (0.5 mM) and pNPP (10 mM) in MeCN/aq. buffer (pH 5, 2.4 K, 9.376664 GHz). Nonpolar hydrogen atoms have been omitted from the structures for clarity.

initially increase with temperature, plateau, and subsequently decrease (see the Supporting Information). This is characteristic of an antiferromagnetically coupled dinuclear Fe^{III} complex in which the exchange coupling constant, J [see Eq. (1)], is greater than the zero-field splitting, D , that is, a strong exchange regime exists ($|J| > |D|$) and this produces a spin ladder ($S_{\text{tot}}=0, 1, 2, 3, 4, 5$) in which the $S_{\text{tot}}=0$ state has the lowest energy. For coupled-spin systems, which exhibit a distribution of zero-field splitting, the EPR spectra typically arise from an $S_{\text{tot}}=3$ spin state as the spin projection operators^[21] for the other spin states are very large and result in broadening of the resonances.^[22–28] Computer simulations, assuming a strong exchange regime ($|J| > |D|$) and performed by using the XSophe-Sophe-XeprView computer simulation software suite and an $S=3$ effective spin Hamiltonian, incorporating only the zero-field splitting and electron Zeeman interactions (not shown), reproduced some of the resonant field positions and intensities around $g_{\text{eff}}=2$, but not all and particularly not those at lower magnetic

fields. This is not surprising as an examination of the temperature dependence of the resonances around $g=2$ (see the Supporting Information) revealed that these resonances arise from transitions within the $S_{\text{tot}}=1, 2$, and 3 spin states. Consequently, we employed a total spin Hamiltonian (H_{tot}) for a coupled diferric system that incorporates the fine structure and electron Zeeman interactions for each center as well as the isotropic and anisotropic exchange interactions [dipole–dipole and spin–orbit contributions, Eq. (1)]. Computer simulation of the EPR spectra of $[(\text{H}_2\text{L})\{\text{Fe}^{\text{III}}_2(\text{O})\}(\text{Cl}_4)]^{2+}$ with an excess of pNPP or phosphate, performed by using the coordinates determined in the DFT calculations, J_{iso} from the variable-temperature measurements, and the g and D values listed in Table 2, produced the spec-

Table 2. Simulated (Molecular Sophe)^[29,30] and computed (DFT) parameters of the EPR spectra of $[(\text{H}_2\text{L})\text{Fe}_2\text{OCl}_4]^{2+}$ with phosphate or pNPP in MeCN/aq. buffer.

Parameter	$[(\text{H}_2\text{L})\text{Fe}_2\text{OCl}_4]^{2+}$ + phosphate		$[(\text{H}_2\text{L})\text{Fe}_2\text{OCl}_4]^{2+}$ + pNPP	
	Simulated	Computed	Simulated	Computed
g_{iso} ^[a]	2.01	--	1.99	--
D [cm^{-1}] ^[a]	217×10^{-4} ^[b]	--	185×10^{-4} ^[c]	--
E/D ^[a]	0.33	--	0.33	--
$d(\text{Fe}\cdots\text{Fe})$ [\AA]	4.57 ^[d]	4.54	4.60 ^[e]	4.68
J_{iso} [cm^{-1}] ^[f]	1.59	5.22	1.76	6.22

[a] Equal for both Fe^{III} centers. [b] The x and z principal components of D are rotated by $\beta = \pm 40^\circ$ for each Fe^{III} center. [c] The x and z principal components of D are rotated by $\beta = \pm 35^\circ$ for each Fe^{III} center. [d] The atomic coordinates for Fe(1) and Fe(2) are $x,y,z=0,0,0$ and $4.57,0,0$ [\AA], respectively. [e] The atomic coordinates for Fe(1) and Fe(2) are $x,y,z=0,0,0$ and $4.60,0,0$ [\AA], respectively. [f] $H=JS_1S_2$

tra (blue line) shown in Figure 3. Importantly, although the magnitudes of J and D (see Table 2) are consistent with the strong exchange regime ($|J| > |D|$), they are in the range of the microwave quantum, resulting in many additional transitions. For example, a resonance is observed at $g_{\text{eff}} \sim 4.3$, which is reproduced in the simulated spectra of the diiron centers (Figure 3). Inspection of the variable-temperature slice (see the Supporting Information) reveals that this resonance arises in part from a formerly forbidden transition within the $|\pm 1\rangle$ doublet (as reflected in the hump around 3 K, which is typical of an antiferromagnetically coupled center) and a small proportion of mononuclear high-spin Fe^{III} .

$$H_{\text{tot}} = \sum_{i=1}^2 (\vec{S}_i D \vec{S}_i + \beta \vec{B} g \vec{S}_i) + J_{\text{iso}} \vec{S}_1 \vec{S}_2 + \vec{S}_1 J \vec{S}_2 \quad (1)$$

In the case of the phosphomonoester, two pNPP molecules coordinate to one complex unit (derived from ^{31}P NMR titrations, see the Supporting Information), which, in combination with the simulated and calculated EPR parameters (Table 2), leads to the structural proposal shown in Figure 3b. Evans' NMR measurements ($\mu_{\text{eff}}=4.71$ B.M.) indicate that only a fraction of the molecules are present in this form. We suggest, in addition, the presence of a strongly

antiferromagnetically coupled μ -oxo-bridged complex with two phosphomonoester molecules, which results in an EPR-silent ($S_{\text{tot}}=0$) species. The dihydroxo species in Figure 3b is then the result of a hydrolyzed oxo bridge. In the case of phosphate, very similar EPR parameters were obtained and, in combination with ^{31}P NMR titrations, the structure shown in Figure 3a is proposed. In contrast, the EPR spectrum of $[(\text{H}_2\text{L})\{\text{Fe}^{\text{III}}_2(\text{O})\}(\text{Cl}_4)]^{2+}$ with the phosphodiester diphenyl phosphate (DPP) is significantly different, showing only a weak signal at $g_{\text{eff}}=4.3$, which can be attributed to uncoupled high-spin ferric ions that are formed by hydrolysis of the μ -oxo-bridged species. Therefore, no additional bridging by the diester is expected because this should lead to similar signals to those shown in Figure 3.

Mössbauer spectra were recorded of frozen solutions of 1) $[(\text{H}_2\text{L})\{\text{Fe}^{\text{III}}_2(\text{O})\}(\text{Cl}_4)]^{2+}$ in MeCN/aqueous buffer (1:1, pH 5), 2) the catalyst solution (1) after the addition of 2 equiv of pNPP, and 3) the catalyst solution (1) after the addition of 2 equiv of DPP; the spectra were recorded at various temperatures with and without an applied external field (3 or 5 T). Relevant spectra are shown in Figures 4 and 5, and the parameters derived from fits to these and other spectra are given in Table 3 (see the Experimental Section and Supporting Information for more). As expected from the UV/Vis, NMR, ESI-MS, and EPR experiments (see Scheme 4 and Figures 1–3), all the Mössbauer spectra are mixtures of three or more species. 1) One subspectrum from each experiment has two very strongly antiferromagnetically coupled high-spin Fe^{III} centers; these A-type species are EPR silent and assigned to singly oxo-bridged diferric complexes with a very strong Heisenberg exchange interaction, $J > 150 \text{ cm}^{-1} \gg |D|$, and relatively large and negative values of the electric field gradient ΔE_{O} . 2) A second subspectrum (type B) is due to a diferric species with weaker (moderate-to-strong) exchange coupling and positive values for ΔE_{O} . These spectra may be due to dinuclear complexes with mixed oxo-hydroxo- or dihydroxo bridges. The estimated exchange coupling for this type of diferric complex is $120 > J > 80 \text{ cm}^{-1}$, that is, $J \gg |D|$. These species were also relevant in PAP and corresponding models and, expected, they are EPR silent.^[2] 3) A third type of subspectra (type C) is due to (pseudo)monomeric high-spin Fe^{III} complexes (uncoupled or very weakly coupled diferric systems, for example, phosphate/phosphoester-bridged or monomeric high-spin Fe^{III} complexes^[31,32]). Similarly to the B-type spectra, the observed ΔE_{O} values are positive. The exchange coupling ranges from intermediate ($J > |D|$) to very weak ($J \sim |D|$), and these are the only species that are EPR-active. Therefore the corresponding Mössbauer subspectra were fitted with J and D values and the atomic coordinates of the Fe^{III} centers (dipole-dipole interaction) derived from the EPR measurements and simulations. All spectra consist of around 50% of an A-type species (large negative ΔE_{O} , small line widths with Voigt-type line shapes). Low-temperature exchange-coupled (see Figure 5 and Table 3). For the catalyst alone (diiron(III) complex without added substrate), this must

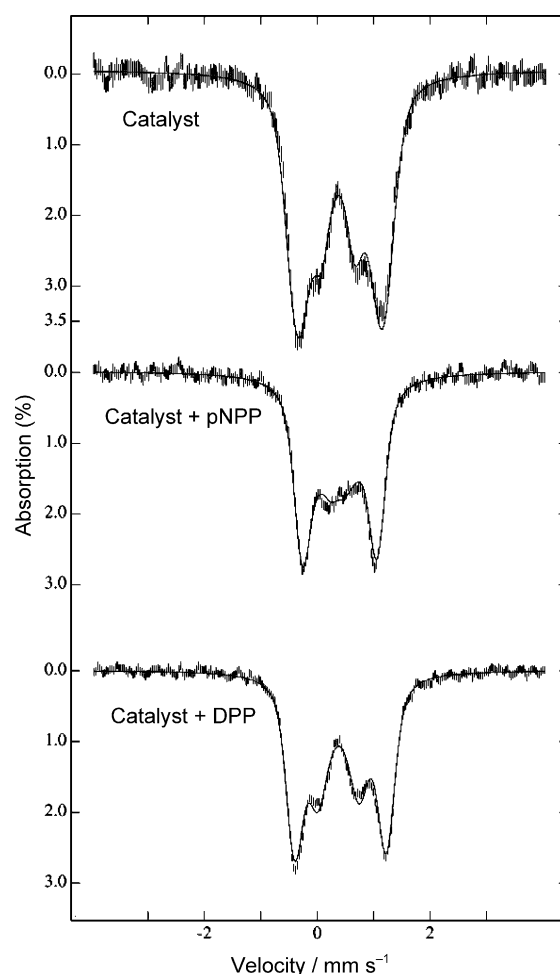


Figure 4. Mössbauer spectra recorded at 3 K without an applied magnetic field. Top: ^{57}Fe -enriched samples of $[(\text{H}_2\text{L})\{\text{Fe}^{\text{III}}_2(\text{O})\}(\text{Cl}_4)]^{2+}$ (2 mm, 1:1 MeCN/aq. buffer, pH 5; δ and ΔE_{O} in mms^{-1}): Type A (57%): $\delta=0.51$, $\Delta E_{\text{O}}=-1.52$; type B (27%): $\delta=0.48$, $\Delta E_{\text{O}}=0.69$; type C (18%): $\delta=0.48$, $\Delta E_{\text{O}}=0.57$. Middle: sample from the top with added pNPP (4 mm): Type A (50%): $\delta=0.50$, $\Delta E_{\text{O}}=-1.29$; type B (20%): $\delta=0.49$, $\Delta E_{\text{O}}=0.23$; type C (30%): $\delta=0.49$, $\Delta E_{\text{O}}=0.58$. Bottom: sample from the top with added DPP (4 mm): Type A (50%): $\delta=0.52$, $\Delta E_{\text{O}}=-1.64$; type B (10%): $\delta=0.49$, $\Delta E_{\text{O}}=0.52$; type C (40%): $\delta=0.49$, $\Delta E_{\text{O}}=0.82$.

result from any of the oxo-bridged structures from Scheme 4 ($[(\text{H}_2\text{L})\{\text{Fe}^{\text{III}}_2(\text{O})\}(\text{OH}_n)_2]^{m+}$, $n=1, 2$). The isomer shifts of the two A-type spectra with pNPP and DPP added are very similar to that of the pure catalyst, which suggests that all three complexes have a similar structure, that is, intact oxo bridges, which is in agreement with the other spectroscopic data and DFT-based studies. However, upon reaction with the monodentate substrate DPP or the bidentate pNPP, there are significant changes in the quadrupole splitting ($\Delta E_{\text{O}}=-1.5$ (catalyst alone) vs. -1.6 (DPP) vs. -1.3 mms^{-1} (pNPP)), and this indicates that the $\text{Fe}^{\text{III}}\cdots\text{Fe}^{\text{III}}$ distances change significantly. Based on literature data,^[33] we assume that there is a significant increase in the $\text{Fe}^{\text{III}}\cdots\text{Fe}^{\text{III}}$ distance of the A-type species with the bidentate substrate. This is supported by the DFT-based analysis (see Figure 1) and results from the phosphate bridge. With the monodentate sub-

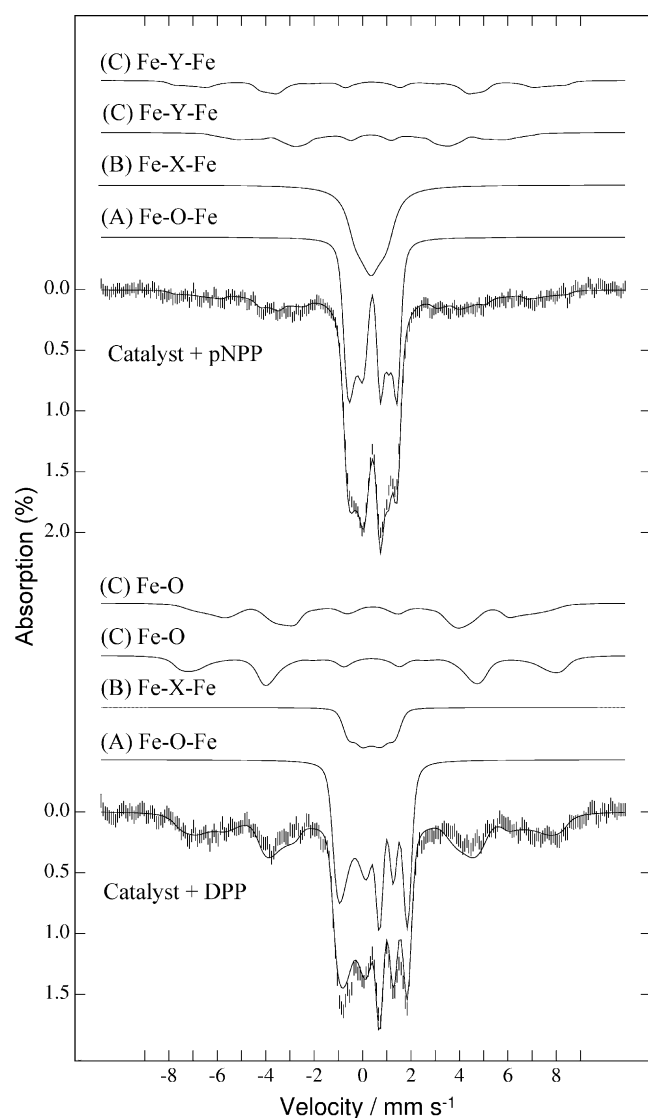


Figure 5. Mössbauer spectra of the middle and bottom samples of Figure 4 (that is, $[(\text{H}_2\text{L})\{\text{Fe}^{\text{III}}_2(\text{O})\}(\text{Cl})_4]^{2+}$ with added pNPP (top) or DPP (bottom)) recorded at 2.2 K in a perpendicular external field of 3 and 5 T, respectively (δ and ΔE_{O} in mm s^{-1} , J in cm^{-1}). Top: Type A (50%): $\delta = 0.50$, $\Delta E_{\text{O}} = -1.34$, $J > 7$; type B (25%): $\delta = 0.47$, $\Delta E_{\text{O}} = 0.63$, $J > 7$; type C (25%): $\delta = 0.47$, $\Delta E_{\text{O}} = 0.23$, $J = 0.5$. Bottom: Type A (50%): $\delta = 0.52$, $\Delta E_{\text{O}} = -1.64$, $J = 180$; type B (11%): $\delta = 0.49$, $\Delta E_{\text{O}} = 0.63$, $J > 120$; type C (40%): $\delta = 0.49$, $\Delta E_{\text{O}} = 0.82$, $J \sim 0.2$.

strate, the shift of the quadrupole splitting is significantly smaller and towards a more negative value, which suggests a small decrease in the $\text{Fe}^{\text{III}}\cdots\text{Fe}^{\text{III}}$ distance, in agreement with the NMR and UV/Vis data, that is, the phosphodiester DPP coordinates to the Fe^{III} centers without the formation of phosphodiester bridges. The B-type subspectra have significantly weaker but still intermediate-to-strong exchange interactions between the two Fe^{III} centers. However, these complexes have positive ΔE_{O} values (see Table 3). We assume that the ferric ions of the B centers are doubly bridged, and oxo-hydroxo- or dihydroxo-bridged diferric complexes might account for the observed parameter values

Table 3. Fitted parameters for the Mössbauer spectra recorded at $T = 2.2$ K with and without an applied magnetic field.^[a]

Type	Sample	δ [mm s^{-1}] ^[b]	ΔE_{O} [mm s^{-1}] ^[c]	J [cm^{-1}]	Γ [mm s^{-1}] ^[d]	Area [%]
A	catalyst	0.51	-1.52	150 ^[e]	-0.43	50
	+DPP	0.52	-1.64	180	-0.35	50
	+pNPP	0.50	-1.34	>7	-0.29	50
B	catalyst	0.48	0.69	>120 ^[e]	0.64	30
	+DPP	0.49	0.63	>120	0.65	11
	+pNPP	0.47	0.63	>7	0.6	25
C	catalyst	0.48	0.57	~ 0.2 ^[e]	0.4	20
	+DPP	0.49	0.82	~ 0.2	0.65	40
	+pNPP	0.47	0.23	0.5	0.45	25

[a] The results from variable field conditions are included in the table as measurements or estimations of the exchange parameter J for each subspectra type. Variable temperature leads to linear second-order Doppler shifts with a typical value of -0.02 mm s^{-1} for an increase in temperature of 60 K. [b] Relative to elemental Fe at room temperature. [c] Negative ΔE_{O} values result from spectra recorded in a strong applied field. [d] A negative sign for line widths denotes Voigt line shapes. [e] Estimated value (see text).

(see Table 3). This assignment is also in agreement with expectations based on the observed $\text{p}K_{\text{a}}$ values (see below) and, as expected for a dihydroxo-bridged complex, these subspectra remain nearly unchanged after the addition of DPP or pNPP. The third kind of Mössbauer subspectra (type C) is characterized by extremely weak or absent exchange coupling between the ferric ions, that is, largely magnetically isolated metal centers. This is in agreement with cleaved oxo bridges (see Scheme 4). At a very low temperature these species exhibit, even at zero magnetic field, a characteristic magnetic sextet (see Figure 5). Successful fits are achieved with a coupled spin Hamiltonian with $J \sim |D|$ (see Table 3),^[34,35] but also with two single spin Hamiltonians with $S = 5/2$ when allowing for several anisotropies. Between the weakly coupled C-type subspectrum of the pure catalyst and that after addition of pNPP, there is a significant decrease in the quadrupole splitting ($\Delta E_{\text{O}} = 0.2$ vs. 0.6 mm s^{-1}), but there is a much smaller change when DPP is added ($\Delta E_{\text{O}} = 0.8 \text{ mm s}^{-1}$). Following a similar reasoning to that suggested above for the A-type subspectra, we assume that these spectra result from the presence of an unbridged diferric complex in the hydrolyzed catalyst, that is, $[(\text{H}_2\text{L})\{\text{Fe}^{\text{III}}(\text{OH})_2(\text{OH}_2)_4\}_2]^{4+}$ (see Scheme 4), a phosphomonoester-bridged diferric complex when pNPP is added (see also EPR spectroscopy, Figure 2, and Table 1, $\text{Fe}^{\text{III}}\cdots\text{Fe}^{\text{III}} \sim 4.7 \text{ \AA}$), and an unbridged diferric site when DPP is the substrate (see EPR spectroscopy above). Spectra were also recorded at a higher temperature (120 K) for the system with added DPP, allowing the determination of the exchange coupling constants J . For the oxo-bridged species (type A), there is a strong antiferromagnetic coupling with $J^{\text{A}}(\text{DPP}) = 180 \text{ cm}^{-1}$. Not unexpectedly, for the B-type species with a predicted moderate-to-strong antiferromagnetic interaction (see above), $J^{\text{B}}(\text{DPP})$ is still large but significantly smaller than for the oxo-bridged complex ($> 120 \text{ cm}^{-1}$). For all A-type species a negative quadrupole splitting is found (see above) with the typical shape of 2–3 absorption

resonance lines for spectra recorded in strong applied fields, which indicates a surplus of charge along the EFG (electric field gradient) z axis. This is in agreement with our assumption that the variation in ΔE_Q is proportional to the $\text{Fe}^{\text{III}}\cdots\text{Fe}^{\text{III}}$ distance alone when the z axis of the EFG and the $\text{Fe}^{\text{III}}\cdots\text{Fe}^{\text{III}}$ axes are collinear. With shorter bridges, the quadrupole splitting becomes more negative and the complexes show very strong antiferromagnetic coupling. On the other hand, with longer bridges the quadrupole splitting assumes more and more positive values as the coupling between the high-spin Fe^{III} centers decreases. For the spectra resulting from the coordination of pNPP, no field spectra were recorded at higher temperatures and, therefore, only the lower limits of the superexchange parameters are available (see the Supporting Information).

Analysis of all the spectroscopic data leads to a consistent interpretation and allows for the following conclusions: In MeCN/aq. buffer mixtures, the complexes of $[(\text{H}_2\text{L})\{\text{Fe}^{\text{III}}_2(\text{O})(\text{Cl}_4)\}^{2+}$ and the adducts with pNPP and DPP are present in three forms. There are strongly antiferromagnetically coupled μ -oxo-bridged complexes (species A), which are EPR silent and give rise to signals with a large negative quadrupole splitting in the Mössbauer spectra. Partial hydrolysis leads to dihydroxo- (or oxo-hydroxo-) bridged species with intermediate-to-strong antiferromagnetic coupling (species B), which are also EPR silent. Hydrolysis of the hydroxo or dihydroxo bridges leads to largely uncoupled diferric complexes (species C). There are striking differences between the adducts of pNPP or DPP and the A-type species: Upon reaction with pNPP there probably is a single phosphoester bridge with a relatively small $\text{Fe}^{\text{III}}\cdots\text{Fe}^{\text{III}}$ distance, and with DPP more than one of the substrates is coordinated, leading to an elongation of the $\text{Fe}^{\text{III}}\cdots\text{Fe}^{\text{III}}$ distance. DPP is possibly monodentately coordinated to only one ferric ion, whereas the phosphomonoester pNPP is bound to both metal ions in a bridging mode (μ - η^1 , η^1). Although this entire analysis is self-consistent, the combination of experiments reported here does not allow for a completely unambiguous interpretation of the complex equilibria. However, it clearly provides a valuable basis for the mechanistic study discussed below.

Kinetics and mechanistic studies: The activity of $[(\text{H}_2\text{L})\{\text{Fe}^{\text{III}}_2(\text{O})(\text{X})_n\}^{m+}$ ($n \leq 4$, $\text{X} = \text{Cl}$, OH_2 , OH , solvent, substrate) towards hydrolysis of the activated phosphodiester bis(2,4-dinitrophenyl) phosphate (BDNPP)^[36] and the phosphomonoester DNPP^[37] was investigated by a spectrophotometric assay (the released 2,4-dinitrophenolate has an intense absorption at $\lambda = 400$ nm ($\epsilon = 12100 \text{ M}^{-1} \text{ cm}^{-1}$)). Hydrolysis experiments with BDNPP were conducted according to published procedures:^[11,38–40] BDNPP ($c_0 = 5$ mM) and $[(\text{H}_2\text{L})\{\text{Fe}^{\text{III}}_2(\text{O})(\text{Cl}_4)\}^{2+}$ ($c_0 = 0.04$ mM) were allowed to react in MeCN/buffer at 25 °C. For the substrate- and catalyst-dependent measurements, their concentrations were varied. The Michaelis–Menten diagrams are shown in Figure 6a, the pH profiles are given in Figure 7 (solid line), and the corresponding derived data are listed in Table 4.

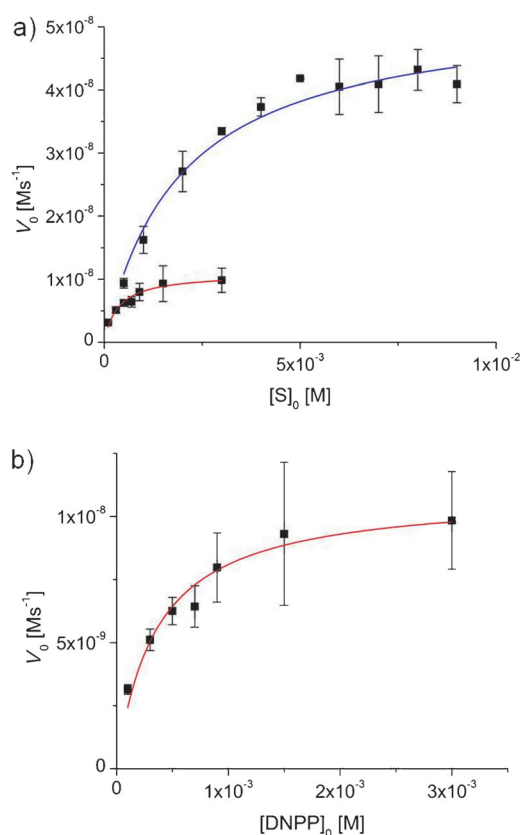


Figure 6. a) Michaelis–Menten diagrams (pH 6) for the rates of hydrolysis of BDNPP (5 mM, blue line) and DNPP (0.5 mM, red line) with $[(\text{H}_2\text{L})\{\text{Fe}^{\text{III}}_2(\text{O})(\text{Cl}_4)\}^{2+}$ (0.04 mM) and b) enlarged diagram of the DNPP hydrolysis reaction. The experimental data are shown as black squares, the lines represent fits to Equation (2).

Table 4. Kinetic parameters of $[(\text{H}_2\text{L})\{\text{Fe}^{\text{III}}_2(\text{O})(\text{Cl}_4)\}^{2+}$.

Substrate	pH _{max}	k_{cat} [10 ⁻³ s ⁻¹]	K_M [mM]	k_{cat}/K_M [M ⁻¹ s ⁻¹]	pK _a [I] ^[a]	pK _a [II] ^[a]
BDNPP	6.17	1.33 ± 0.08	1.94 ± 0.37	0.68 ± 0.02	5.0 ± 0.1	7.3 ± 0.1
DNPP	6.09	0.27 ± 0.02	0.35 ± 0.07	0.78 ± 0.03	5.7 ± 0.3	6.3 ± 0.4

[a] The deprotonation steps pK_a(I) and pK_a(II) leading to the active species are shown in Scheme 4.

$$V_0 = \frac{V_{\text{max}}[S]_0}{K_M + [S]_0} \quad (2)$$

$$V_0 = V_{0,\text{max}} \frac{\left(1 + \frac{\gamma K_a(2)}{[\text{H}^+]}\right)}{\left(1 + \frac{[\text{H}^+]}{K_a(1)} + \frac{K_a(2)}{[\text{H}^+]}\right)} \quad (3)$$

The catalytic activity k_{cat} is approximately half the value of the most active diiron PAP mimetics ($[(\text{L}')\text{Fe}^{\text{III}}_2(\mu\text{-OAc})_2]^{2+}$: $k_{\text{cat}} = 3.5 \times 10^{-3} \text{ s}^{-1}$, $K_M = 8.70$ mM, $k_{\text{cat}}/K_M = 0.40 \text{ M}^{-1} \text{ s}^{-1}$ with $\text{L}' = N$ -(2-hydroxybenzyl)- N -(2-hydroxy-5-methyl-3-[(2-pyridylmethyl)amino]methyl)benzyl)aminoacetic acid,^[8] the heterovalent $[(\text{L}'')\text{Fe}^{\text{III}}(\mu\text{-OAc})_2\text{Fe}^{\text{II}}]^{+}$ complex: $k_{\text{cat}} = 3.0 \times 10^{-3} \text{ s}^{-1}$, $K_M = 13.00$ mM, $k_{\text{cat}}/K_M = 0.23 \text{ M}^{-1} \text{ s}^{-1}$ with $\text{L}'' = 2$ -bis[(2-pyridylmethyl)aminomethyl]-6-[(2-hydroxybenzyl)(2-pyridylmethyl)aminomethyl]-4-methylphenol^[41]),

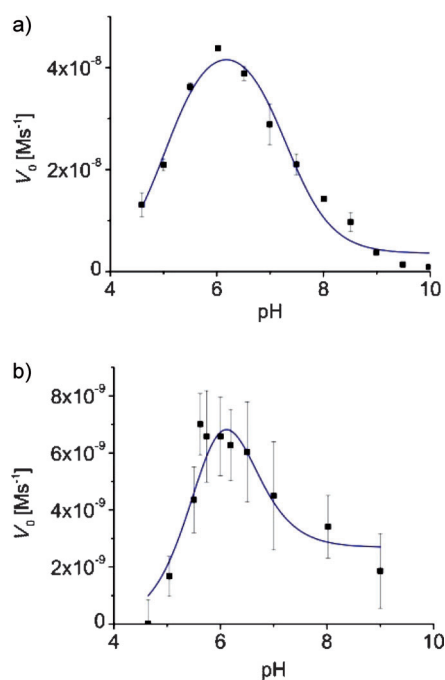


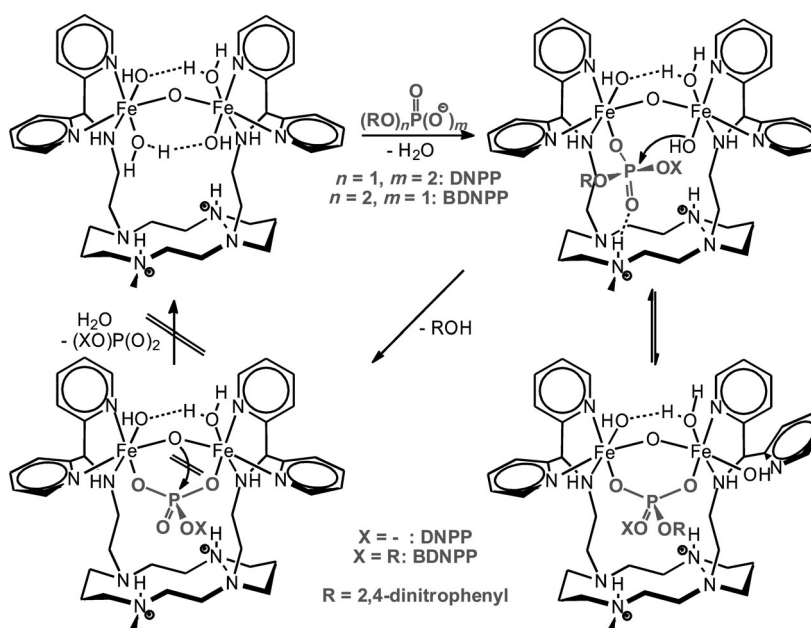
Figure 7. pH profiles for the rates of hydrolysis of a) BDNPP (5 mM) and b) DNPP (0.5 mM) with $[(L)[\text{Fe}^{\text{III}}(\text{Cl})_2(\text{O})]$ (0.04 mM). The experimental data are shown as black squares, the blue lines represent the fits to Equation (3). The factor γ in Equation (3) describes the observed plateau of activity at high pH. The large error bars in (b) originate from the low substrate concentration and, therefore, the low observed activity in the hydrolysis of DNPP.

but the relatively low Michaelis–Menten constant of $K_M = 1.94$ mM leads to the highest catalytic efficiency k_{cat}/K_M reported so far. Stoichiometric experiments followed by ^{31}P NMR spectroscopy showed no release of hydrolyzed phosphate although the production of 2,4-dinitrophenol was observed spectrophotometrically (1 equiv of 2,4-dinitrophenolate was released). It follows that the hydrolysis product (DNPP) remains bound to $[(\text{H}_2\text{L})\{\text{Fe}^{\text{III}}_2(\text{O})\}(\text{X})_n]^{m+}$ and inhibits catalysis. The cyclam-based ligand H_2L^{2+} was designed to stabilize DNPP in a monodentate coordination mode for long enough and in a high enough concentration to allow nucleophilic attack by a terminal hydroxide. Hydrolysis experiments with DNPP were therefore conducted in a similar way as for BDNPP but with a 10-fold lower substrate concentration ($c_0 = 0.5$ mM; at higher concentration autohydrolysis leads

to saturation kinetics). Indeed, hydrolysis of the phospho-monoester was observed; the results are presented in Figures 6 and 7 and in Table 4.^[42] $[(\text{H}_2\text{L})\{\text{Fe}^{\text{III}}_2(\text{O})\}(\text{X})_n]^{m+}$ accelerates the reaction by a factor of 1.45 (pH 6, 0.5 mM DNPP), the typical bell-shaped pH profile is observed, and the resulting pH maximum and $\text{p}K_a$ values (see Table 4) suggest the same active species and a very similar mechanism to that observed with BDNPP (see Scheme 5). As discussed above, diferric model systems such as $[(\text{H}_2\text{L})\{\text{Fe}^{\text{III}}_2(\text{O})\}(\text{X})_n]^{m+}$ usually coordinate phosphates and phosphoesters in a bridging mode.^[43,44] Indeed, the relatively inactive monoester *p*-nitrophenyl phosphate (pNPP) may coordinate in this way (see Figure 3) and therefore is not hydrolyzed. That is, the secondary interactions do not, as expected (see Figure 1, Scheme 5), entirely prevent the bridging mode but lead to subtle changes in the equilibria and possible pathways.

Conclusion

$[(\text{H}_2\text{L})\{\text{Fe}^{\text{III}}_2(\text{O})\}(\text{X})_n]^{m+}$ is the first PAP mimic that hydrolyzes monoester substrates, albeit with a relatively low activity in comparison with the observed diesterase activity.^[38–40,45,46] Note, however, that the catalytic efficiency (k_{cat}/K_M) with the monoester substrate is comparable to that with the diester substrate (see Table 2), and this is due to the relatively tight binding due to secondary interactions. This unusual reactivity, which models the biological function of PAP, has been attributed to secondary interactions due to the protonated cyclam platform (Scheme 5) and supports well the catalytic mechanism proposed for PAP enzymes, that is, a monodentate coordination of the phosphoester fol-



Scheme 5. Proposed reaction mechanism for the hydrolysis of BDNPP and DNPP with $[(\text{H}_2\text{L})\{\text{Fe}^{\text{III}}_2(\text{O})\}(\text{OH})_2(\text{OH}_2)_2]^{4+}$.

lowed by nucleophilic attack of a terminal or free hydroxide.^[12,46]

Experimental Section

Synthesis of L: 1,8-Dimethylcyclam^[47] (1.00 g, 4.38 mmol) was dissolved in dry MeCN (30 mL). The solution was heated at reflux and *N*-tosylaziridine^[48,49] (2.10 g, 10.66 mmol) in dry MeCN (30 mL) was added dropwise. The reaction mixture was heated at reflux for 6 h, the solvent was removed in vacuo, and the residue recrystallized in hot DCM/EtOH (1:1) to yield 1,8-bis(2-tosylaminoethyl)-4,11-dimethylcyclam as a tan powder (1.80 g, 66%). 1,8-Bis(2-tosylaminoethyl)-4,11-dimethylcyclam (1.00 g, 1.61 mmol) and conc. H₂SO₄ (7.5 mL) were heated at 100 °C for 48 h and then the reaction mixture was added dropwise to diethyl ether. The resulting white precipitate was filtered off and washed with diethyl ether, dissolved in water (20 mL), and 3 M NaOH solution was added until the solution reached pH 14. The product was extracted with chloroform (5 × 15 mL), the organic phase was dried over Na₂SO₄, and the solvent was removed in vacuo to yield 1,8-bis(2-aminoethyl)-4,11-dimethylcyclam as a yellowish oil (0.50 g, 100%). 1,8-Bis(2-aminoethyl)-4,11-dimethylcyclam (0.45 g, 1.43 mmol), di-2-pyridylmethyl chloride^[50] (0.60 g, 2.86 mmol), and potassium carbonate (0.41 g, 2.86 mmol) were dissolved in dry MeCN under argon and heated at reflux for 24 h. After cooling, the reaction mixture was poured into water (60 mL) and sodium hydroxide was added until the solution reached pH 14. The product was extracted with ethyl acetate (3 × 50 mL), the organic phase was dried over K₂CO₃, and the solvent removed in vacuo. The crude product was purified by column chromatography (neutral alumina, chloroform/methanol 99:1 to 95:5), and the resulting oil crystallized from hot hexane to yield pale-yellowish crystals (0.24 g, 26%). ¹H NMR (400 MHz, CDCl₃): δ = 8.53 (dd, ³J_{H,H} = 4.8, ⁴J_{H,H} = 1.2 Hz, 4H; CH_{Ar}N), 7.60 (dt, ³J_{H,H} = 8.0, ⁴J_{H,H} = 1.2 Hz, 4H; CH_{Ar} para to N), 7.48 (d, 4H; CH_{Ar,q}), 7.10 (ddd, ³J_{H,H} = 8.0, ³J_{H,H} = 4.8, ⁴J_{H,H} = 1.2 Hz, 4H; CH_{Ar}CHN), 5.06 (s, 2H; CHPy₂), 3.12 (br s, 2H; NH), 2.7–2.2 (m, 24H; all N-CH₂), 2.11 (s, 6H; N-CH₃), 1.47 ppm (quint., ³J_{H,H} = 6.8 Hz, 4H; C-CH₂-C); ¹³C NMR (100 MHz, CDCl₃): δ = 161.9 (C_{Ar,q}), 149.2, 136.5, 122.2, 122.0 (C_{Ar}), 70.3 (CHPy₂), 54.5, 54.3, 53.9, 51.7, 50.8 (all N-CH₂), 45.7 (CH₂-NH), 43.5 (N-CH₃), 24.1 ppm (C-CH₂-C); IR (KBr): $\tilde{\nu}$ = 3439 (b), 3282 (m), 2981 (m), 2937 (m), 2846 (m), 2792 (s), 1674 (s), 1565 (s), 1599 (m), 1473 (s), 1466 (s), 1435 (s), 1294 (m), 1162 (m), 1125 (m), 1114 (m), 999 (w), 929 (m), 887 (w), 809 (m), 771 cm⁻¹ (m). MS (FAB⁺, Nibeol): *m/z* (%): 651.6 (97) [M+H]⁺; elemental analysis calcd (%) for C₃₈H₅₄N₁₀·H₂O: C 68.23, H 8.44, N 20.94; found: C 68.69, H 8.43, N 21.05.

Synthesis of [(H₂L)Fe₂OCl₄](Cl)₂: Ligand L (195 mg, 0.30 mmol) and [FeCl₄](NET₄)^[19] (197 mg, 0.60 mmol) were separately dissolved in MeCN (30 and 3 mL, respectively) and the solutions then combined while stirring. The resulting ochre precipitate was collected on a filter, washed with cold MeCN, and dried in vacuo (215 mg, 67%). IR (KBr): $\tilde{\nu}$ = 3439 (b), 2964 (w), 2859 (w), 1608 (s), 1593 (w), 1471 (s), 1449 (s), 1290 (w), 1158 (w), 1052 (w), 1022(m), 831 (m), 817 (m), 769 cm⁻¹ (m); UV/Vis (MeCN, 1% H₂O): λ_{\max} (ϵ) = 256 (48470), 315 (sh, 23783), 378 (16450), 480 (sh, 900), 600 nm (143 M⁻¹cm⁻¹); HRMS (ESI⁺, MeCN, 1% H₂O): *m/z* (%): 921.19821 (calcd 921.19838) (100) [HLFe^{III}₂Cl₄O]⁺, 883.22483 (calcd 883.22439) (69) [LFe^{III}Cl₃O]⁺, 741.35780 (calcd 741.35709) (14.6) [LFe^{II}Cl]⁺; elemental analysis calcd (%) for C₃₈H₅₄N₁₀OFe₂Cl₄·5H₂O·2HCl: C 68.23, H 8.44, N 20.94, Cl 19.63, Fe 10.48; found: C 68.69, H 8.43, N 21.05, Cl 18.63, Fe 10.51.

Kinetic measurements for BDNPP and DNPP hydrolysis: Phosphatase activity for the activated diester substrate BDNPP was determined in acetonitrile/buffer (1:1) at 25 °C between pH 4.6 and 10. Product formation (2,4-dinitrophenolate) was observed spectrophotometrically at 400 nm. To determine the initial activity, the time between 30 and 240 s was analyzed by linear regression. A multicomponent buffer was used containing MES, HEPES, and CHES (all 50 mM) and LiClO₄ (250 mM) in MilliQ water. The pH was adjusted to the desired value with aq. NaOH. The complex and substrate solutions were prepared separately in MeCN

and their final concentrations in the cuvette were 0.04 and 5 mM, respectively. These were varied in the cases of complex and substrate dependency measurements. The substrate-dependency data were fitted by using the Michaelis–Menten equation [Eq. (2)]. The resulting pH profiles were fitted with the Origin 8.1G software package (Origin Lab Corporation, www.OriginLab.com) by using Equation (3) for a diprotic system with two active species.^[51] Phosphatase activity for the activated monoester substrate DNPP was determined in a similarly to the BDNPP assays with the following alterations: DNPP was dissolved in buffer of the desired pH. The final concentration in the cuvette was 0.5 mM. Autohydrolysis rates were determined prior to as well as directly after the two catalytic measurements at each pH. Spectral changes that affected the rates due to ligand exchange at the complex were also recorded and subtracted at the end.

DFT calculations: DFT geometry optimizations were performed with the Gaussian 03 software package^[52] by using the B3LYP functional,^[53,54] the TZVP^[55,56] basis set on iron and phosphorus, and the SVP^[55,56] basis set on carbon, hydrogen, nitrogen, and oxygen. The optimized structures were confirmed as minima by frequency calculations on the PES and reported energies are zero-point corrected. The relaxed PES scans on [(H₂L)Fe^{III}₂(O))(OH)₂(OH₂)(DNPP)] ($x=2, 0$) were performed with the Gaussian 09 software package^[57] with the B3LYP functional,^[57] the LanL2Dz^[58] basis set, and the PCM solvation model^[59] with acetonitrile as solvent. The minimum structures of the starting points were confirmed by frequency calculations.

IR spectroscopy: IR measurements were performed with a Perkin–Elmer 16 PC FT-IR spectrometer in KBr. Signal intensities are abbreviated as followed: b = broad, w = weak, m = medium, s = strong.

Electron absorption spectroscopy: UV/Vis spectra and time-course measurements at fixed wavelengths were recorded on a JASCO V-570 spectrophotometer equipped with a JASCO ETC-505T cryostat at 25 °C. Time-dependent UV/Vis measurements were performed by using a TIDAS II J&M spectrophotometer. The baseline was recorded prior to a measurement series using pure solvent and subtracted automatically. Fast processes were monitored by stopped-flow measurements using an Applied Photophysics PD.1 photodiode array stopped-flow spectrophotometer. A linear 256 element diode array APL xenon lamp served as the light source. For recording and handling the data, the software suite !XScan 1.09 by P.J. King (AP Ltd. 1995) was used.

NMR spectroscopy: Solution magnetic moments were determined by using the Evans NMR method.^[53] A capillary containing [D₃]MeCN was placed in an NMR tube containing [D₃]MeCN and the [(H₂L){Fe^{III}₂(O)-(Cl₄)²⁺} complex with pNPP. The NMR spectrum was measured at 400 MHz and the paramagnetic shifted solvent peak was used to calculate the magnetic moment of the dinuclear complex. ¹H, ¹³C, and ³¹P NMR spectra were measured on a Bruker Biospin Avance II 400 instrument.

EPR spectroscopy: Liquid helium temperature X-band EPR spectra (about 9 GHz) were recorded on a Bruker Biospin Elexsys E580 spectrometer equipped with a Super High Q cavity and an Oxford Instruments ESR 910 cryostat with an ITC503 temperature controller at 1.8 to 16 K. The microwave frequency and magnetic field were calibrated with a Bruker frequency counter and a Bruker ER036 TM Tesla meter. Spin Hamiltonian parameters were determined from computer simulation of the experimental spectra using the XSophe-Sophe-XeprView^[54] and Molecular Sophe^[29] computer simulation software suites. The simulated and experimental spectra were visualized with Xepr.

Mössbauer spectroscopy: The Mössbauer spectra of the frozen solutions were acquired with a conventional spectrometer in the constant-acceleration mode equipped with a ⁵⁷Co source (3.7 GBq) in a rhodium matrix. Isomer shifts are given relative to α -Fe at room temperature. The frozen samples were inserted in an Oxford Instruments Mössbauer-Spectromag 4000 cryostat, which has a split-pair superconducting magnet system for applied fields of up to 5 T with the field of the sample oriented perpendicular to the γ -ray direction; the sample temperature was varied between 3.0 and 300 K. WMOSS (www.wmoss.org) was used for the spectral simulations. To minimize the parameter set the single-spin Hamiltonian given by Equation (4) was used for the analysis.

$$H = D \left[\hat{S}_z^2 - \frac{1}{3} S(S+1) + \frac{E}{D} (\hat{S}_x^2 - \hat{S}_y^2) \right] + \mu_B \vec{S} \vec{g} \vec{B}_0 + \{ \vec{S} \} A I - g_N \mu_N \vec{B}_0 \vec{I} + H_{\text{electric}} \quad (4)$$

To avoid overparametrization, a conservative fit procedure was assumed: When possible, a typical range of parameter values from the literature was assumed.^[33, 60–62] Various arrangements of group-fit spectra on carefully chosen categories of parameters were used to check the consistency of the model throughout the fit procedure and for the various magnetic fields and temperatures. The values for the g tensor and zero-field splitting parameters D and E/D are those emerging from the EPR spectra and simulations. Consistent with the observation that $S = \pm 5/2$ Kramers doublet is the ground state (electronic part of the spin Hamiltonian), D is assumed to be negative. To check for the consistency of the parameters, a coupled-spin Hamiltonian was also used (not shown here). The exchange parameters were determined by using the coupled-spin Hamiltonian with a Heisenberg exchange term (JS_1S_2 ; WMOSS uses the convention that $J > 0$ for antiferromagnetic exchange) and summation over the electronic states of the coupled system.

Acknowledgements

Financial support by the German Science Foundation (DFG) is gratefully acknowledged.

- [1] D. E. Wilcox, *Chem. Rev.* **1996**, *96*, 2435.
- [2] N. Mitić, S. J. Smith, A. Neves, L. W. Guddat, L. R. Gahan, G. Schenk, *Chem. Rev.* **2006**, *106*, 3338.
- [3] M. Krauss, *J. Chem. Inf. Comput. Sci.* **2001**, *41*, 8.
- [4] F. Zheng, C.-G. Zhan, R. L. Ornstein, *J. Phys. Chem. B* **2002**, *106*, 717.
- [5] D. E. C. Ferreira, W. B. DeAlmeida, A. Neves, W. R. Rocha, *Phys. Chem. Chem. Phys.* **2008**, *10*, 7039.
- [6] M. E. Alberto, T. Marino, M. J. Ramos, N. Russo, *J. Chem. Theory Comput.* **2010**, *6*, 2424.
- [7] R. Than, A. A. Feldmann, B. Krebs, *Coord. Chem. Rev.* **1999**, *182*, 211.
- [8] L. R. Gahan, S. J. Smith, A. Neves, G. Schenk, *Eur. J. Inorg. Chem.* **2009**, 2745.
- [9] G. Schenk, T. W. Elliott, E. Leung, L. E. Carrington, N. Mitić, L. R. Gahan, L. W. Guddat, *BMC Struct. Biol.* **2008**, *8*, 6.
- [10] Y.-S. Yang, J. M. McCormick, E. I. Solomon, *J. Am. Chem. Soc.* **1997**, *119*, 11832.
- [11] M. Lanznaster, A. Neves, A. J. Bortoluzzi, V. V. E. Aires, B. Szpoganicz, H. Terenzi, P. C. Severino, J. M. Fuller, S. C. Drew, L. R. Gahan, G. R. Hanson, M. J. Riley, G. Schenk, *J. Biol. Inorg. Chem.* **2005**, *10*, 319.
- [12] N. Mitić, K. S. Hadler, L. R. Gahan, A. C. Hengge, G. Schenk, *J. Am. Chem. Soc.* **2010**, *132*, 7049.
- [13] N. Sträter, T. Klabunde, P. Tucker, H. Witzel, B. Krebs, *Science* **1995**, *268*, 1489.
- [14] T. Klabunde, N. Sträter, R. Frohlich, H. Witzel, B. Krebs, *J. Mol. Biol.* **1996**, *259*, 737.
- [15] E. G. Funhoff, W. L. Wang, G. Andersson, B. A. Averill, *FEBS J.* **2005**, *272*, 2968.
- [16] In general, dinucleating ligands for PAP model complexes include a phenolate as part of the ligand backbone to model the hydroxo bridge; secondary interactions to position the substrate have not been included in model systems so far.
- [17] M. Dietrich, D. Münstermann, H. Suerbaum, H. Witzel, *Eur. J. Biochem.* **1991**, *199*, 105.
- [18] Due to two pK_a values of around 9 for the first two protonation steps and pK_a values of around 3 for the third and fourth protonations of 1,4,8,11-tetramethylcyclam,^[19] we assume that L and the diferric complex of L are doubly protonated at pH values between approx. 3 and 9, that is in the pH range of PAP activity.
- [19] N. S. Gill, *J. Chem. Soc.* **1961**, 3512.
- [20] Note that there are some ambiguities in terms of the exact assignment of all species. However, in general, the ³¹P NMR titrations fully support the data discussed here and they also suggest that, as expected, the coordination modes strongly depend on the pH and the particular substrate used.
- [21] A. Bencini, D. Gatteschi, *EPR of Exchange Coupled Systems*, Springer, Berlin, **1990**.
- [22] N. Mitić, C. J. Noble, L. R. Gahan, G. R. Hanson, G. Schenk, *J. Am. Chem. Soc.* **2009**, *131*, 8173.
- [23] A. Ozarowski, B. R. McGarvey, J. E. Drake, *Inorg. Chem.* **1995**, *34*, 5558.
- [24] Note that D_e and D_c are large and of opposite sign, which allows the observation of resonances from the $S=2$ and $S=3$ spin states of the dinuclear Fe^{III} complex.
- [25] E. Bill, U. Beckmann, K. Wieghardt, *Hyperfine Interact.* **2002**, *144*, 183.
- [26] V. A. Grillo, G. R. Hanson, D. Wang, T. W. Hambley, L. R. Gahan, K. S. Murray, B. Moubaraki, C. J. Hawkins, *Inorg. Chem.* **1996**, *35*, 3568.
- [27] S. J. W. Holgate, G. Bondarenko, D. Collison, F. E. Mabbs, *Inorg. Chem.* **1999**, *38*, 2380.
- [28] S. J. Smith, R. A. Peralta, R. Jovito, A. Horn Jr, C. J. Noble, G. R. Hanson, R. Stranger, V. Jayaratne, G. Cavigliasso, L. R. Gahan, G. Schenk, O. R. Nascimento, A. Cavalett, T. Bortolotto, G. Razzera, H. Terenzi, A. Neves, M. J. Riley, *Inorg. Chem.* submitted.
- [29] G. R. Hanson, C. J. Noble, S. Benson, in *High Resolution EPR: Applications to Metalloenzymes and Metals in Medicine*, Vol. 28 (Eds.: G. R. Hanson, L. J. Berliner), **2009**, p. 105.
- [30] MoSophe includes Boltzmann factors for the energy levels in its calculations.
- [31] P. Comba, G. Linti, M. Zajackowski-Fischer, T. Zessin, *J. Incl. Phen.* **2011**, *71*, 331.
- [32] In addition to the *syn* conformation of the two dipyrldylamine binding sites discussed here, there also is a possible *anti* conformation with longer metal–metal distances; this *anti* conformation has been observed in the metal-free ligand.^[31] Monomeric metal complexes in which the two dipyrldylamine donors coordinate to only one metal ion have also been observed but there is no evidence for these monomeric complexes in the high-spin Fe^{III} complexes studied here.^[31]
- [33] H. Zheng, Y. Zang, Y. Dong, V. G. Young Jr., L. Que Jr, *J. Am. Chem. Soc.* **1999**, *121*, 2226.
- [34] J. T. Sage, P. G. Debrunner, *Hyperfine Interact.* **1986**, *29*, 1399.
- [35] Because a weak antiferromagnetic exchange interaction for high-spin diferric species ($J \sim |D|$) can be simulated with a single-spin Hamiltonian formalism by allowing anisotropic contributions to the A tensor,^[34] we report in this paper the two (pseudo)monomeric (single-spin Hamiltonian) values, which share the same set of parameters but have differing Euler angles for the A matrix and the EFG (electric field gradient) tensor (see the Supporting Information, Table S4). The sum of the two (pseudo)monomeric contributions will therefore represent the total contribution of the weakly coupled dinuclear complexes for the B-type geometries. One can qualitatively judge the value of the exchange terms between the two Fe^{III} centers by looking at the anisotropy of the A matrix. The reported J values were, however, determined by studying the temperature dependence of the spectra of samples under a strong magnetic field by using an appropriate coupled-spin Hamiltonian (see the Experimental Section).
- [36] C. A. Bunton, S. J. Farber, *J. Org. Chem.* **1969**, *34*, 767.
- [37] G. Rawji, R. M. Milburn, *J. Org. Chem.* **1981**, *46*, 1205.
- [38] M. Lanznaster, A. Neves, A. J. Bortoluzzi, B. Szpoganicz, E. Schwingel, *Inorg. Chem.* **2002**, *41*, 5641.
- [39] P. Karsten, A. Neves, A. J. Bortoluzzi, M. Lanznaster, V. Drago, *Inorg. Chem.* **2002**, *41*, 4624.
- [40] S. C. Batista, A. Neves, A. J. Bortoluzzi, I. Vencato, R. A. Peralta, B. Szpoganicz, V. V. E. Aires, H. Terenzi, P. C. Severino, *Inorg. Chem. Commun.* **2003**, *6*, 1161.

- [41] A. Neves, M. A. Debrito, V. Drago, K. Griesar, W. Haase, *Inorg. Chim. Acta* **1995**, *237*, 131.
- [42] The low substrate concentration is responsible for the low observed activity and the large errors (see the Supporting Information for experimental details).
- [43] R. E. Norman, S. P. Yan, L. Que jr., G. Backes, J. S. Ling, J. Sanders-Loehr, J. H. Zhang, C. J. O'Connor, *J. Am. Chem. Soc.* **1990**, *112*, 1554.
- [44] P. N. Turowski, W. H. Armstrong, S. C. Liu, S. N. Brown, S. J. Lipard, *Inorg. Chem.* **1994**, *33*, 636.
- [45] R. S. Cox, G. Schenk, N. Mitic, L. R. Gahan, A. C. Hengge, *J. Am. Chem. Soc.* **2007**, *129*, 9550.
- [46] A. Neves, M. Lanznaster, A. J. Bortoluzzi, R. A. Peralta, A. Casellato, E. E. Castellano, P. Herrald, M. J. Riley, G. Schenk, *J. Am. Chem. Soc.* **2007**, *129*, 7486.
- [47] G. Royal, V. Dahaoui-Gindrey, S. Dahaoui, A. Tabard, R. Guillard, P. Pullumbi, C. Lecomte, *Eur. J. Org. Chem.* **1998**, 1971.
- [48] D. B. Hope, K. C. Horncastle, *J. Chem. Soc. C* **1966**, 1098.
- [49] A. E. Martin, T. M. Ford, J. E. Bulkowski, *J. Org. Chem.* **1982**, *47*, 412.
- [50] G. Roelfes, V. Vrajmasu, K. Chen, R. Y. N. Ho, J. Rohde, C. Zonder van, R. M. la Crois, E. P. Schudde, M. Lutz, A. L. Spek, R. Hage, B. Feringa, E. Munck, L. Que Jr., *Inorg. Chem.* **2003**, *42*, 2639.
- [51] I. H. Segel, *Enzyme Kinetics—Behavior and Analysis of Rapid Equilibrium and Steady-State Enzyme Systems*, Wiley, New York, **1975**.
- [52] M. J. Frisch, G. W. Trucks, H. B. Schlegel, G. E. Scuseria, M. A. Robb, J. R. Cheeseman, J. A. Montgomery Jr., T. Vreven, K. N. Kudin, J. C. Burant, J. M. Millam, S. S. Iyengar, J. Tomasi, V. Barone, B. Mennucci, M. Cossi, G. Scalmani, N. Rega, G. A. Petersson, H. Nakatsuji, M. Hada, M. Ehara, K. Toyota, R. Fukuda, J. Hasegawa, M. Ishida, T. Nakajima, Y. Honda, O. Kitao, H. Nakai, M. Klene, X. Li, J. E. Knox, H. P. Hratchian, J. B. Cross, V. Bakken, C. Adamo, J. Jaramillo, R. Gomperts, R. E. Stratmann, O. Yazyev, A. Austin, R. Cammi, C. Pomelli, J. W. Ochterski, P. Y. Ayala, K. Morokuma, G. A. Voth, P. Salvador, J. J. Dannenberg, V. G. Zakrzewski, S. Dapprich, A. D. Daniels, M. C. Strain, O. Farkas, D. K. Malick, A. D. Rabuck, K. Raghavachari, J. B. Foresman, J. V. Ortiz, Q. Cui, A. G. Baboul, S. Clifford, J. Cioslowski, B. B. Stefanov, G. Liu, A. Liashenko, P. Piskorz, I. Komaromi, R. L. Martin, D. J. Fox, T. Keith, M. A. Al-Laham, C. Y. Peng, A. Nanayakkara, M. Challacombe, P. M. W. Gill, B. Johnson, W. Chen, M. W. Wong, C. Gonzalez, J. A. Pople, Gaussian 03, Revision E.01, Gaussian Inc., Wallingford CT, **2004**.
- [53] A. D. Becke, *Phys. Rev. A* **1988**, *38*, 3098.
- [54] C. Lee, W. Yang, R. G. Parr, *Phys. Rev. B* **1988**, *37*, 785.
- [55] A. Schäfer, H. Horn, R. Ahlrichs, *J. Chem. Phys.* **1992**, *97*, 2571.
- [56] A. Schäfer, C. Huber, R. Ahlrichs, *J. Chem. Phys.* **1994**, *100*, 5829.
- [57] M. J. Frisch, G. W. Trucks, H. B. Schlegel, G. E. Scuseria, M. A. Robb, J. R. Cheeseman, G. Scalmani, V. Barone, B. Mennucci, G. A. Petersson, H. Nakatsuji, M. Caricato, X. Li, H. P. Hratchian, A. F. Izmaylov, J. Bloino, G. Zheng, J. L. Sonnenberg, M. Hada, M. Ehara, K. Toyota, R. Fukuda, J. Hasegawa, M. Ishida, T. Nakajima, Y. Honda, O. Kitao, H. Nakai, T. Vreven, J. A. Montgomery Jr., J. E. Peralta, F. Ogliaro, M. Bearpark, J. J. Heyd, E. Brothers, K. N. Kudin, V. N. Staroverov, R. Kobayashi, J. Normand, K. Raghavachari, A. Rendell, J. C. Burant, S. Iyengar, J. Tomasi, M. Cossi, N. Rega, N. J. Millam, M. Klene, J. E. Knox, J. B. Cross, V. Bakken, C. Adamo, J. Jaramillo, R. Gomperts, R. E. Stratmann, O. Yazyev, A. J. Austin, R. Cammi, C. Pomelli, J. W. Ochterski, R. L. Martin, K. Morokuma, V. G. Zakrzewski, G. A. Voth, P. Salvador, J. J. Dannenberg, S. Dapprich, A. D. Daniels, O. Farkas, J. B. Foresman, J. V. Ortiz, J. Cioslowski, D. J. Fox, *Revision A.02*, Gaussian, Inc., Wallingford CT, **2009**.
- [58] T. H. Dunning Jr., P. J. Hay in *Modern Theoretical Chemistry*, Vol. 3 (Ed.: H. F. Schaefer III), Plenum Press, New York, **1976**, p. 1.
- [59] J. Tomasi, B. Mennucci, R. Cammi, *Chem. Rev.* **2005**, *105*, 2999.
- [60] B. G. Fox, M. P. Hendrich, K. K. Surerus, K. K. Andersson, W. A. Froland, J. D. Lipscomb, E. Münck, *J. Am. Chem. Soc.* **1993**, *115*, 3688.
- [61] B. A. Averill, J. C. Davis, S. Burman, T. Zirino, J. Sanders-Loehr, T. M. Loehr, J. T. Sage, P. G. Debrunner, *J. Am. Chem. Soc.* **1987**, *109*, 3760.
- [62] X. Zhang, H. Furutachi, S. Fujinami, S. Nagatomo, Y. Maeda, Y. Watanabe, T. Kitagawa, M. Suzuki, *J. Am. Chem. Soc.* **2005**, *127*, 826.

Received: January 21, 2011

Revised: September 26, 2011

Published online: January 10, 2012